IEEE Access
Multidisciplinary | Rapid Review | Open Access Journal

Received 13 September 2023, accepted 26 September 2023, date of publication 29 September 2023,
date of current version 10 October 2023.

Digital Object Identifier 10.1109/ACCESS.2023.3320932

RESEARCH ARTICLE

Theoretical Model of Tangential Contact Stiffness and Damping of Solid-Liquid Interface in Macroscopic Relative Motion

LIXIA PENG[1,2], ZHAOYANG BAN[1], ZHIQIANG GAO[1], WEIPING FU[1,2], FENG GAO[1], AND WEN WANG[1]

[1]School of Mechanical and Precision Instrument Engineering, Xi'an University of Technology, Xi'an 710048, China
[2]School of Engineering, Xi'an International University, Xi'an 710077, China

Corresponding author: Weiping Fu (weipingf@xaut.edu.cn)

This work was supported in part by the National Natural Science Foundation of China under Grant 52005401, in part by the China Postdoctoral Science Foundation under Grant 2019M663782, in part by the Shaanxi Natural Science Basic Research Project under Grant 2020JQ-629, and in part by the Special Scientific Research Project of Shaanxi Provincial Department of Education under Grant 20JK0800.

ABSTRACT The macroscopic relative motion solid-liquid interface widely exists in the contact motion pairs of machine tools and other mechanical equipment. In order to accurately obtain the tangential contact stiffness and damping parameters, the Savkoor asperity adhesion-sliding friction contact model is used to analyze the contact area and the corresponding tangential force changes of a single pair of solid contact asperity in the four typical phases of contact growth, contact stagnation, crack adhesion and crack propagation. According to the hypothesis of Gaussian distribution of asperity on rough surface, the contact model of single-pair asperities is extended to the whole joint. The tangential contact stiffness and damping models of solid-solid interface in macroscopic relative motion are obtained. For the fluid contact part, the oil film pressure distribution and film thickness are obtained by solving part of the film Reynold's equation, and then the fluid tangential stiffness and damping model is established. The tangential contact stiffness and damping of the whole solid-liquid interface are obtained by analyzing the stiffness and damping of solid and fluid parts, and the effects of normal load and moving velocity on tangential contact stiffness and damping are obtained by simulation. The results show that the tangential contact stiffness and damping of solid-liquid interface increase with the increase of normal contact load and decrease with the increase of moving velocity.

INDEX TERMS Solid-liquid interface, relative motion, tangential direction, contact stiffness, contact damping.

I. INTRODUCTION

In machine tools and other kinds of mechanical equipment, there are a large number of joints which are in direct contact and can produce relative motion, such as machine tool sliding guideway joint, bearing roller and inner and outer ring joint, gear transmission joint, and so on. When these pairs move in a linear or rotary motion, there is generally a lubricating medium in the contact surface, which forms a relatively moving solid-liquid interface, and its tangential contact stiffness and damping are nonlinear and time-variable. It is very important in the friction dynamics analysis of various drive systems, and is considered to be one of the most important influencing factors of vibration and noise [1]. In particular, there are common tangential dynamic contact characteristics such as friction vibration, creeping phenomenon and insufficient transmission stiffness of the motion pair in the machine tool movement and machining process [2], [3], [4], which not only exert a great impact on the machining performance, but also directly affect the stability of the system, even causing the instability of the system [5], [6], [7], [8]. Thus, it can be seen that the tangential contact stiffness and damping of the macroscopic relative motion solid-liquid interface are important parameters that affect

The associate editor coordinating the review of this manuscript and approving it for publication was Jingang Jiang.

the dynamic performance of the whole machine. Therefore, it is necessary to model accurately, reveal its asperity contact mechanism, and explore its influencing factors and laws.

Cattaneo and Mindlin took the lead in solving the tangential action problem of nonlinear ball-surface contact, analyzed the tangential stiffness and energy dissipation of the interface, and established a Mindlin local sliding model with tangential stick-slip characteristics [9], [10]. So far, the tangential contact problem of the bonding surface has been widely concerned about, and the statistical model and fractal model based on rough surface have been gradually formed [11], [12], [13], [14], [15], [16], [17]. With the development of elastohydrodynamics theory, more and more attention has been paid to the influence of lubricating media on the contact characteristics of rough surfaces. Huifang et al. [18] established the normal stiffness model of solid contact by statistical model, measured the liquid stiffness by ultrasonic reflection coefficient method, and then, through coupling, obtained the static normal stiffness of mixed lubrication joint. Sun et al. [19] derived the expression of liquid stiffness based on ultrasonic spring model, thin film resonance model and Taylor approximate equation, and established a two-dimensional (2D) fractal model of static normal stiffness of mixed lubrication joints. Li et al., Wen et al. [20], [21], [22] used the Three-dimensional Fractal Theory to characterize the rough surface, established the contact stiffness model of solid surface based on statistical method, and established the stiffness model of oil film by solving the equivalent thickness of oil film. As a result, the Three-dimensional Fractal Model of normal static stiffness of the joint under mixed lubrication was obtained. Gao et al. [23] combined theoretical analysis and experimental verification to solve the problem of solid-liquid interface stiffness and damping modeling of normal harmonic vibration under mixed lubrication. Zhou et al. [24] and [25] proposed a tangential stiffness and damping model by considering the coupling of gear stiffness and damping and oil film stiffness and damping. Peng et al. [26] established a model of tangential stiffness and damping of solid-liquid interface when normal static load and tangential harmonic vibration occur, and thus verified it by experiments. Dwyer-Joyce et al. [27] measured the normal contact stiffness of lubricating steel balls from static, mixed to full-film state when sliding on the steel disk by ultrasonic reflection method, and found that with the increase of sliding velocity, the contribution of liquid stiffness to the total stiffness gradually increased, and even became the main part, even in the static state, the liquid stiffness also contributed to the total stiffness. Peng et al. [28] obtained the equivalent normal dynamic stiffness of dry friction and oil lubrication system of sliding guideway system by peak resonance method. The simulation results show that the increase of sliding velocity will decrease the normal dynamic stiffness of the bonding surface. When the contact surface bears a large pressure or there is lubrication, the velocity has little effect on the normal dynamic stiffness. The studies mentioned above mainly focus on the tangential contact parameters without considering lubrication or normal contact parameters without lubrication, and seldom involve the tangential contact parameters of macroscopic relative motion joint under lubrication condition.

The relative movement of solid-liquid interface causes very serious nonlinear friction characteristics [29]. Researchers mostly examined this problem from the tribological point of view of sliding contact behavior. Jackson et al. [30] used semi-analytical and finite element simulation methods to analyze the average tangential force and normal force produced by the sliding interaction between two asperities, and established the empirical equation. Korayem et al. [31], [32], [33] established the contact mechanics model of micro-scale nanoparticles, deduced the calculation formulas of surface adhesion force and friction force, and discussed the effects of adhesion force in different contact models on the indentation depth and contact angle between tip and substrate of nanoparticles. Through numerical simulation of the dynamics and deformation process of nanoparticles, the critical force and critical time of rolling, sliding, stick-slip and rotation of nanoparticles were obtained. Shisode et al. [34] established a friction model under mixed lubrication, considering the influence of sheet metal and tool surface morphology on lubrication pressure distribution, and using fluid mechanics and boundary friction coupling model to determine the overall friction caused by solid-solid asperity contact and lubricating oil pressure. As for Shi et al. [35], in order to study the thermo-mechanical contact between an elastic-plastic sphere and a rigid plate, a simulation was carried out with a slip rate of 0.1m/s to 10m/s. The results show that the sliding friction coefficient and friction stress are significantly related to the sliding rate, while the maximum static friction coefficient has nothing to do with the sliding rate. In addition, the energy release from complete viscosity to complete slip is equivalent to the shear crack energy of the material. Patil et al. [36] used the finite element model to simulate the sliding initiation process of a rigid plate on a deformable sphere under normal and tangential loads. Under the combined action of plasticity, crack propagation and interface slip, the sliding initiation is regarded as the loss of tangential contact stiffness. Chang [37] proposed a deterministic model of partial elastohydrodynamic lubrication (EHL), which can simulate the basic process of asperity interaction and solid-solid contact on rough surfaces under the combined action of elastohydrodynamic lubrication and elastohydrodynamic lubrication. This is the first attempt to establish a deterministic model of friction contact under the mixed state of asperity-elastohydrodynamic lubrication and boundary lubrication. Hu and Wei [38] studied the friction model of two rough surfaces covered by the boundary film. A group of spherical asperities with the same radius of curvature and Gaussian height distribution were used to simulate the rough surface, the shear force of the asperity on the boundary film was expressed by linear equation, and the possibility of the asperity being cut off was considered. The friction behavior was studied by analyzing the influence

of boundary film and surface morphology under different values. These studies solve the problems of adhesion, energy loss, crack generation and friction changes caused by elastic deformation in the process of sliding contact between two rough surfaces under various lubrication conditions, thus providing invaluable conclusions and methods for the study of tangential stiffness and damping of solid-liquid interface. However, there is a lack of direct analysis and modeling of tangential contact stiffness and damping.

With the solid-liquid interface of mixed lubrication in macroscopic relative motionin as the research object, based on Savkoor's [39] sliding friction adhesion model, this article deduced the temporal variation relationships among the tangential force, tangential contact stiffness and normal contact load of a pair of contact asperities in four typical periods of contact growth, contact stagnation, bonding fracture and crack propagation, and the law of the change of contact parameters of a pair of contact asperities in the state of macroscopic relative motion is revealed. Then, using the statistical theory, the contact model of a single pair of asperities is extended to the whole interface, and from the macro level, the tangential contact stiffness/damping model of the solid part of the relative motion solid-liquid interface is obtained. By solving the fluid Reynolds equation, the stiffness and damping of the fluid part are obtained, the solid and fluid parts are summed up, and the tangential contact stiffness and damping model of the solid-liquid interface is established. The established model is simulated, the influencing factors and laws are clarified and revealed, the contact characteristics of fluid and solid are compared and analyzed, and the qualitative comparison conclusions are given. The purpose of this article is to provide a reference for improving the performance of the whole machine in the process of mechanical equipment design and manufacturing with lubricating medium.

II. SOLID CONTACT MODEL OF SOLID-LIQUID INTERFACE IN MACROSCOPIC RELATIVE MOTION

According to the load distribution idea of the mixed lubrication interface [18], the external load of the bonding surface is borne by both the fluid lubricating medium and the solid asperity. Therefore, the contact problem of macroscopic relative motion solid-liquid interface under mixed lubrication needs to be modeled from solid and fluid parts respectively.

The solid part needs to start with the asperity model, analyze the change of the actual contact area under the influence of load, and determine the tangential friction force, so that the tangential contact stiffness and damping can be further solved.

A. ASPERITY CONTACT MODEL

In Savkoor [39], according to the basic theory of energy and material balance in the sliding process, experiments are carried out at low velocity under the conditions of kinematic and dynamic constraints imposed on the system, and in order to minimize the complex influence of non-uniform transient flash temperature field related to friction heat dissipation, an asperity sliding contact model of elastic body and rigid body under quasi-isothermal condition is established. It is assumed that there are a large number of asperities between the two contact planes and covered with an adsorption layer, which will break due to sliding friction, but when it is exposed to the atmosphere again, it can be absorbed almost instantly, so that the adsorption layer can be supplemented. In the process of sliding contact, the interaction of asperity goes through four typical phases as shown in Figure 1.

① $0 < t \leq t_s$, Growth phase. This is the initial phase of the interaction of a pair of contact asperities, and the contact area increases with time from the moment of the first point contact ($t = 0$) to the stagnant point ($t = t_s$). The adhesive friction causes the surface profile of the asperity to produce elastic deformation, and the shear strain also increases.

② $t_s < t \leq t_m$, Stagnation phase. Starting from time t_s, the sliding contact begins to stagnate, and the shear force at the boundary of the contact area begins to increase rapidly, and the contact area reaches the maximum at ($t = t_m$).

③ $t_m < t \leq t_i$, Crack adhesion phase. This is a short transition phase, and the relative displacement between the asperities leads to the further increase of the shear traction strength until the crack at the bonding of ($t = t_i$).

④ $t_i < t \leq 2t_m$, Crack propagation phase. The crack propagates steadily, which leads to the destruction of the adsorption layer, and at this time ($t = 2t_m$) the contact of this pair of asperities ends.

In the contact process, according to the Theory of Adhesion, the normal load affects the sliding friction indirectly only through its influence on the actual contact area. The geometric structure of the asperity interaction is shown in Figure 2. Let R_1 and R_2 be the radius of two contact asperities, the central indentation is α, the relative moving velocity is V, and the central distance between two asperities is s, the time t is calculated from the moment $s = s_m$ that the contact is established at the first point, when the central indentation reaches the maximum value α_m the indentation begins to decrease, until $2t_m$, the contact ends.

For convenience, a coordinate system is added to each of the two asperities. Figure 3 shows the size and relative position of the contact area measured along X_2 relative to the $X_2 - Z_2$ coordinate system. The L and T in the figure represent the position of the contact leading edge and the contact trailing edge respectively. At different contact phases, the interaction between the two asperities is reflected in the change of their size and the position of the contact leading edge and the contact trailing edge. Since the inclination of typical contact between rough surfaces of nominal smooth surfaces is usually very small, it is assumed that their effects on the normal and tangential components of the contact force can be ignored.

In the contact process, according to the Theory of Adhesion, the normal load affects the sliding friction indirectly only through its influence on the actual contact area. The geometric structure of the asperity interaction is shown in

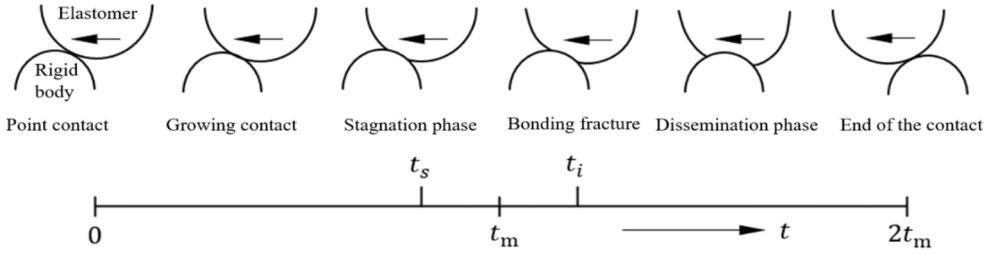

FIGURE 1. Interaction between a pair of asperities in different phases of adhesive contact.

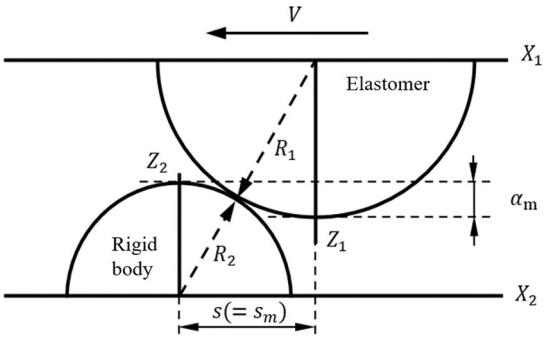

FIGURE 2. Geometry of interaction of asperity.

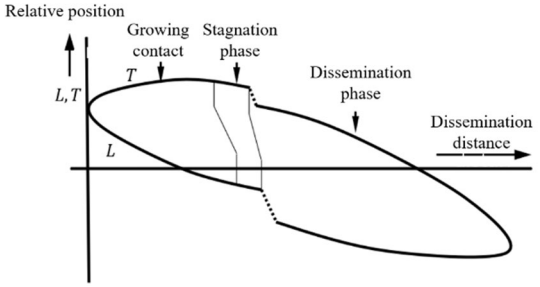

FIGURE 3. The Contact area and position of asperity at each phase.

Figure 2. Let R_1 and R_2 be the radius of two contact asperities, the central indentation is α, the relative moving velocity is V, and the central distance between two asperities is s, the time t is calculated from the moment $s = s_m$ that the contact is established at the first point, when the central indentation reaches the maximum value α_m the indentation begins to decrease, until $2t_m$, the contact ends.

1) NORMAL CONTACT LOAD IN THE WHOLE CONTACT PHASE

Referring to Figure 2 above, we can approximately estimate the directional load and contact area. Assuming that the problem is a pure normal indentation problem, the indentation depth varies with time in the same way as in the case of friction-free sliding, and at $0 \le t \le t_m$, α can be written as a function of t.

$$\alpha(t) \approx \frac{V^2 t(2t_m - t)}{4R_m} \tag{1}$$

where $R_m = \frac{R_1+R_2}{2}$, the maximum central indentation $\alpha_m = \alpha(t_m) = \frac{V^2 t_m^2}{4R_m}$.

By quoting Hertz's Theory of Elasticity [40], the radius of the contact circle is $a(t)$, and the contact area and normal load are:

$$a^2(t) = R\alpha(t) = \frac{\psi V^2 t(2t_m - t)}{4} \tag{2}$$

$$P_n(t) = \frac{8}{3R}\int_0^t G(t - t_1)\frac{d}{dt_1}a^3(t_1)dt_1 \tag{3}$$

where $1/R = 1/R_1 + 1/R_2$ and the intermediate parameter $\psi = \frac{R}{R_m}$ characterize the geometric shape of the surface roughness of the asperity; supposing that the elastic properties of the contact surface are the same and isotropic, then E, ν and G are surface elastic modulus, Poisson's ratio and shear modulus, and $E = 3G$ if ν is 0.5, then.

Substituting (2) into (3), obtains

$$P_n(t) = \frac{8\sqrt{R}}{3}[2G]\alpha^{\frac{3}{2}}(t) \tag{4}$$

According to Boltzmann's superposition principle Boltzmann [41], the following is obtained:

$$P_n(t) = \frac{8}{3R}\int_0^t G(t - t_1)\frac{d}{dt_1}a^3(t_1)dt_1 \tag{5}$$

where $G(t) = G_r\frac{1+10^3}{(1+\frac{t}{t_0})^n}$ is the shear relaxation modulus of the contact surface material., G_r is the shear modulus of the contact surface material in the rubber state, and t_0 and n represent the position and span of the transition from rubber state to glass state along the time axis, which is determined by the surface properties of the asperity.

When $t_m \le t \le 2t_m$, the indentation decreases and the contact area decreases accordingly. In the analysis of this attenuation process, we introduced a new time variable $t_D(t)$, which is a function of the current time t, as is shown in Equation (6):

$$a(t) = a\{t_D(t)\}, \quad t \ge t_m, t_D(t) \le t_m \tag{6}$$

Therefore,

$$\int_{t_m}^{t} G(t-t_1)\frac{d}{dt_1}\{\alpha(t_1)\}\,dt_1 = -\int_{t_D(t)}^{t_m} G(t_D(t)-t_1)\frac{d}{dt_1}\{\alpha(t_1)\}\,dt_1 \tag{7}$$

In this case, the contact area and normal load are:

$$a^2(t) = a^2\{t_D(t)\} = \frac{\psi V^2 t_D(t)\{2t_m - t_D(t)\}}{4} \tag{8}$$

$$P_n(t) = \frac{8}{3R}\int_0^{t_D(t)} G(t_D(t)-t_1)\frac{d}{dt_1}a^3(t_1)dt_1 \tag{9}$$

where t_1 is a dummy variable.

Combining (2) and (8), the solution $t_D(t) = 2t_m - t$ is obtained.Substitution of (2) in (5) and (8) in (9) obtains $0 < t \le t_m$, the normal contact load $P_n(t)$ is shown in the following equation:

$$P_n(t) = \frac{V^3 t_m \psi^{1.5}}{R}\int_0^t G(t-t_1)\left(\frac{t_1}{t_m}\right)^{\frac{1}{2}}\left(1-\frac{t_1}{t_m}\right)\left(2-\frac{t_1}{t_m}\right)^{\frac{1}{2}} dt_1 \tag{10}$$

Using Mathmatic software, the analytical solution and the conditions to be satisfied are as follows:

$$\begin{aligned} P_n(t) &= \frac{1}{15Rt_m\sqrt{-\frac{t(t-2t_m)}{t_m^2}}}2002t^2V^3\psi^{1.5}G_r\left(\frac{t_0}{t+t_0}\right)^n\sqrt{4-\frac{2t}{t_m}} \\ &\times\left\{\begin{array}{l} -3t\,\text{AppellF1}\left[\frac{5}{2},n,-\frac{1}{2},\frac{7}{2},\frac{t}{t+t_0},\frac{t}{t+t_0},\frac{t}{2t_m}\right]\cdots \\ +6t_m\,\text{AppellF1}\left[\frac{3}{2},n,-\frac{1}{2},\frac{5}{2},\frac{t}{t+t_0},\frac{t}{2t_m}\right] \end{array}\right\} \\ &\times\left(\frac{t_0}{t}\notin\text{Reals}\left\|\text{Re}\left[\frac{t_0}{t}\right]<-1\right\|\left(\text{Re}\left[\frac{t_0}{t}\right]\ge 0\&\&\frac{t_0}{t}\ne 0\right)\right) \\ &\ldots\&\&\left(\frac{t_m}{t}\notin\text{Reals}\left\|2\text{Re}\left[\frac{t_m}{t}\right]\right\|>1\left\|\text{Re}\left[\frac{t_m}{t}\right]\right\|<0\right) \end{aligned} \tag{11}$$

where Re is the real part, Reals is the real space, && is the logic and, || is the logic or, and AppellF1$[a;b_1,b_2;c;x,y]$ refers to Appell's hypergeo-metric function of two variables [29], as is shown in Equation (12):

$$\sum_{m=0}^{\infty}\sum_{n=0}^{\infty}\frac{(a)_{m+n}(b_1)_m(b_2)_n}{m!n!(c)_{m+n}}x^m y^n,\cdots\cdots|x|<1,|y|<1 \tag{12}$$

When $t_m < t \le 2t_m$, in order to calculate the contact load $P_n(t)$, it is only necessary to replace t in Equations (10) and (11) for $t_D(t)$.

2) TANGENTIAL FRICTION AND STIFFNESS IN THE CONTACT PHASE

As can be seen from Figure 3, the contact area does not grow in an axisymmetric manner, and the contact center moves continuously in the sliding direction until it reaches the stagnation point, which is essentially the eccentric growth of the contact area leading to growth stagnation. In order to simplify the model, however, it is assumed that the growth of the region is axisymmetric and stagnates along the whole boundary of the contact circle. With the increase of time, the tangential force will slowly accumulate in the growth phase. According to Mindlin's [42] interrelationship among shear force, displacement, and the relaxation function of the elastic body, as well as the assumptions mentioned above, the relationship between tangential friction force and time in the growth contact phase is deduced.

(1) Contact growth phase

When $0 < t \le t_s$, the contact area is in the growth phase, and the tangential force $F_g(t)$ [39] is:

$$F_g(t) = \frac{8\sqrt{\psi}}{3}V^2 t_m\int_0^t G(t-t_1)y(t_1)dt_1 \tag{13}$$

where $y(t_1) = \sqrt{(t_1/t_m)(2-t_1/t_m)}$.

Using Mathmatic software, the analytical solution and the conditions to be satisfied are as follows:

Substituting tangential displacement $\xi = Vt$ into Equation (14), as shown at the bottom of the next page, and using the tangential force F_g to derive the displacement ξ, the tangential contact stiffness in the growth period is obtained as follows:

$$\begin{aligned} K_g = \frac{dF_g}{d\xi} &= \frac{16016\sqrt{2\psi}}{9}VG_r\ldots \\ &\times\text{AppellF1}\left[\frac{3}{2},n,-\frac{1}{2},\frac{5}{2},\frac{t}{t+t_0},\frac{t}{2t_m}\right] \\ &\times\left(\frac{t_0}{t+t_0}\right)^n\sqrt{\frac{t}{t_m}t_m} \end{aligned} \tag{15}$$

(2) Contact stagnation phase

When $t_s < t < t_m$, the asperity, experiencing the contact growth phase, arrives at the contact stagnation phase, when the context area remains constant and the tangential force $F_s(t)$ [39] is:

$$F_s(t) = \frac{8\sqrt{\psi}}{3}V^2 t_m\int_0^{t_t} G(t-t_1)y(t_1)dt_1 + \int_{t_t}^t G(t-t_1)y(t_s)dt_1) \tag{16}$$

where $y(t_s) = \sqrt{(t_s/t_m)(2-t_s/t_m)}$.

Using Mathmatic software, the analytical solution and the conditions to be satisfied are as follows:

$$\begin{aligned} F_s(t) = \frac{8008}{3}V^2 t\sqrt{\psi}t_m G_r \\ \times\left[\begin{array}{c} \frac{2\sqrt{2}}{3}\text{AppellF1}\left[\frac{3}{2},n,-\frac{1}{2},\frac{5}{2},\frac{t_s}{t+t_0},\frac{t_s}{2t_m}\right]\cdots \\ \times\left(\frac{t+t_0-t_s}{t_0}\right)^{-n}\left(\frac{t+t_0-t_s}{t+t_0}\right)^n\frac{t_s}{t}\sqrt{\frac{t_s}{t_m}} \\ +\frac{(t_0-(t+t_0-t_s)\left(\frac{t+t_0-t_s}{t_0}\right)^{-n}}{t(-1+n)})\sqrt{\frac{(2t_m-t_s)t_s}{t_m^2}} \end{array}\right] \end{aligned} \tag{17}$$

Substituting tangential displacement $\xi = Vt$ into Equation (17) and using the tangential force F_s(t) to derive the tangential displacement ξ, the tangential contact stiffness in the stagnation phase is obtained as follows:

$$K_s = \frac{dF_s}{d\xi}\frac{8008}{3}V^2 t\sqrt{\psi}t_m G_r \times \left[\begin{array}{c} \frac{2\sqrt{2}}{3}\text{AppelF1}\left[\frac{3}{2}, n, -\frac{1}{2}, \frac{5}{2}, \frac{t_s}{t+t_0}, \frac{t_s}{2t_m}\right]\cdots \\ \times(\frac{t+t_0-t_s}{t_0})^{-n}(\frac{t+t_0-t_s}{t+t_0})^n\frac{t_s}{t}\sqrt{\frac{t_s}{t_m}} \\ +\frac{(t_0-(t+t_0-t_s)(\frac{t+t_0-t_s}{t_0})^{-n}}{t(-1+n)})\sqrt{\frac{(2t_m-t_s)t_s}{t_m^2}} \end{array}\right] \tag{18}$$

(3) Contact crack adhesion phase

When $t_m < t < t_i$, the contact of the asperity is in the crack adhesion phase, which is a short transition, when the tangential force $F_r(t_i)$ [39] is:

$$F_r(t_i) = \frac{4}{3}\sqrt{\psi}G_r V_r^2 t_m^2[\arcsin y_s(t) - y_s(t)(1-y_s(t)^2)^{1/2}\cdots + 2y_s(t)k_s(I_r-1)] \tag{19}$$

where V_r indicates that when the modulus of the material is G_r and the response is completely elastic, the minimum sliding velocity of crack occurs at the bonding site; then defining $I_r = t_i/t_s$ as the crack factor, $k_s = t_s/t_m$ is the stagnation ratio, $t_i = t_m I_r k_s$, and $y_s = y(t_s)$.

Substituting the tangential displacement $\xi_r = V_r t$ into (19), and using the tangential force $F_r(t_i)$ to derive the tangential displacement ξ_r, the tangential contact stiffness in the crack phase is obtained as follows (20), as shown at the bottom of the page.

(4) Contact crack propagation phase

When $t_i < t < 2t_m$, in the propagation phase, the relative motion between the asperities is steadily expanded by the relative velocity of the whole joint. The specific process is shown in Figure 4. The two asperities are combined in the

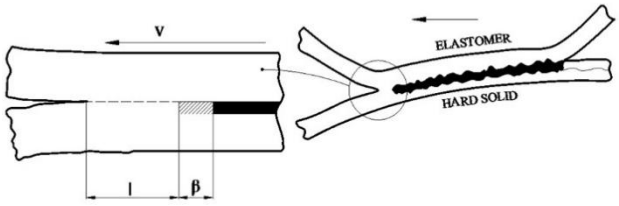

FIGURE 4. Model showing regions of re-adhesion and breakdown at the leading edge of a sliding contact.

region (l). Due to the adhesion, the shear traction force of the asperity increases continuously, and at the exit of this region, the shear traction force increases rapidly, and the strength reaches the finite breakdown traction force τ_B to produce cracks, and further expands to form a crack layer. The bonding zone is approximately regarded as a straight strip with a length of l and a width of πa, and the length of the breakdown zone is β.

According to the local energy balance equation of crack propagation when the velocity is constant as given by Schapery [43], it is inferred that, at the propagation phase of sliding friction, the tangential force $F_p(t)$ [39] is:

$$F_p(t) = \begin{cases} B(V, Vt_m)\left[\bar{t}(2-\bar{t})\right]^{\frac{3}{4}}\cdots\cdots & t_m < t < t_i \\ B(V, Vt_m)\left[\overline{t_D}(2-\overline{t_D})\right]\cdots\cdots & t_i < t < t_{2t_m} \end{cases} \tag{21}$$

where the parameter $\bar{t} = t/t_m$, $\overline{t_D} = t_D/t_m$, $B(V, Vt_m) = G_r\frac{\varepsilon}{\sqrt{\pi}}\frac{\tau_B}{G_r}\psi^{\frac{3}{4}}(Vt_m)^{\frac{3}{2}}[\beta_r\omega(V)]^{\frac{1}{2}}$, the intermediate parameter $\omega(V) = \sqrt[\frac{n-1}{n}]{\frac{3t'_V V}{\beta_r}(\frac{G_g G_r}{1+10^3})^{\frac{1}{n}}}$, $D(t) = \frac{1}{G_g}\frac{1+10^3}{\left(\frac{t'_0}{t}\right)^n}$ is the creep function of an elastic body, $D(\infty) = 1/G_R$, $D(0) = 1/G_g$, and G_r and G_g are the shear moduli of viscoelastomer in rubber state and glass state, usually represented as $G_g/G_r = 10^3$. β_r is the value of β in

$$F_g(t) = \frac{16016}{9}\sqrt{2t}V^2\sqrt{\psi}\text{AppellF1}\left[\frac{3}{2}, n, -\frac{1}{2}, \frac{5}{2}, \frac{t}{t+t_0}, \frac{t}{2t_m}\right]\cdots \times G_r(\frac{t_0}{t+t_0})^n\sqrt{\frac{t}{t_m}}t_m\cdots \times \left(\begin{array}{c} 0<t<t_s \\ \ldots\&\ \&t_s < t_m \\ \ldots\&\ \&(\frac{t_0}{t}\notin \text{Reals}|\text{Re}\left[\frac{t_0}{t}\right] < -1||(\text{Re}\left[\frac{t_0}{t}\right]\geq 0\&\&\frac{t_0}{t}\neq 0))\cdots \\ \&\&(\frac{t_m}{t})\notin \text{Reals}|\left\|2\text{Re}\left[\frac{t_m}{t}\right] > 1\left\|\text{Re}\left[\frac{t_m}{t}\right] < 0\right\|\right. \end{array}\right) \tag{14}$$

$$K_r = \frac{dF_r(t_i)}{d\xi_r} = \frac{4\sqrt{\psi}}{3t}G_r V t_m^2 \times \left[\begin{array}{c} \arcsin\sqrt{\frac{t_s}{t_m}(2-\frac{t_s}{t_m})} - \sqrt{\frac{t_s}{t_m}(2-\frac{t_s}{t_m})}(1-\frac{t_s}{t_m}(2-\frac{t_s}{t_m}))^{1/2} \\ +2\sqrt{\frac{t_s}{t_m}(2-\frac{t_s}{t_m})}k_s(I_r-1) \end{array}\right] \tag{20}$$

rubber state, γ_F is the strength parameter of the adsorption layer, which, together with β_r and τ_B, represent the effects of physical and chemical properties of asperity surface on friction. Among them, γ_F is determined by local energy balance equation $8\gamma_F = \frac{2F_r^2(t_i)}{\pi G_r V_r^3 t_m^3 y_s^3 \psi^{3/2}}$ of crack propagation given by Schapery [43]; as to β_r and τ_B, one is free to be chosen, while the other is determined by $\frac{\pi\gamma_F G_r}{\beta_r \tau_B^2} = 1$. ε is a numerical constant, represented as $\varepsilon = \frac{\pi^2}{2}(\frac{l}{a})^{\frac{1}{2}}$, whose value depends upon the shape of the attenuated traction field and has nothing to do with the sliding velocity and contact area. $t_0{}'$ is a parameter, for the sake of simplification of the representation of $D(t)$, related to t_0. Two time parameters t_0 and t_0' are interrelated by means of the standard convolution integral between $D(t)$ and $G(t)$, which, when substituted into the equation, can be shown as:

$$F_p = \begin{cases} \frac{\varepsilon\tau_B\xi\psi^{\frac{3}{4}}V^{\frac{1}{2}}(t_m)^{\frac{3}{2}}}{t\sqrt{\pi}}\left[\beta_r \sqrt[\frac{n-1}{n}]{\frac{3t_0'V}{\beta_r}(\frac{G_gG_r}{1+10^3})^{\frac{1}{n}}}\right]^{\frac{1}{2}} \cdots \\ \times\left[\frac{t}{t_m(2-\frac{t}{t_m})}\right]^{\frac{3}{4}}, \quad t_m < t < t_i \\ \frac{\varepsilon\tau_B\xi\psi^{\frac{3}{4}}V^{\frac{1}{2}}(t_m)^{\frac{3}{2}}}{t_D(t)\sqrt{\pi}}\left[\beta_r \sqrt[\frac{n-1}{n}]{\frac{3t_0'V}{\beta_r}(\frac{G_gG_r}{1+10^3})^{\frac{1}{n}}}\right]^{\frac{1}{2}} \cdots \\ \times\left[\frac{t_D(t)}{t_m(2-\frac{t_D(t)}{t_m})}\right]^{\frac{3}{4}}, \quad t_i < t < 2t_m \end{cases} \tag{22}$$

Using tangential force F_p to derive its displacement ξ, the tangential contact stiffness K_p in the stagnation phase is obtained as follows:

$$K_p = \begin{cases} \frac{\varepsilon\tau_B\psi^{\frac{3}{4}}V^{\frac{1}{2}}(t_m)^{\frac{3}{2}}}{t\sqrt{\pi}}\left[\beta_r \sqrt[\frac{n-1}{n}]{\frac{3t_0'V}{\beta_r}(\frac{G_gG_r}{1+10^3})^{\frac{1}{n}}}\right]^{\frac{1}{2}} \\ \times\left[\frac{t}{t_m(2-\frac{t}{t_m})}\right]^{\frac{3}{4}}, \quad t_m < t < t_i \\ \frac{\varepsilon\tau_B\psi^{\frac{3}{4}}V^{\frac{1}{2}}(t_m)^{\frac{3}{2}}}{t_D(t)\sqrt{\pi}}\left[\beta_r \sqrt[\frac{n-1}{n}]{\frac{3t_0'V}{\beta_r}(\frac{G_gG_r}{1+10^3})^{\frac{1}{n}}}\right]^{\frac{1}{2}} \\ \times\left[\frac{t_D(t)}{t_m(2-\frac{t_D(t)}{t_m})}\right]^{\frac{3}{4}}, \quad t_i < t < 2t_m, \end{cases} \tag{23}$$

3) NORMAL CONTACT LOAD AND FRICTION THROUGHOUT THE CONTACT PHASE

During the whole contact phase, due to the continuous change of the contact area, the normal contact load and tangential friction of the asperity are constantly changing, but their macroscopic performance is fixed. The average contact load and friction force of each contact phase are regarded as macro normal contact load P_{av} and tangential friction F_{av}

$$P_{av} = \frac{\sum_{t=0}^{t_s} P_n(t)/N_{t_s} + \sum_{t=t_s}^{t_i} P_n(t)/N_{(t_i-t_s)}}{4} \cdots + \frac{P_n(t_i) + \sum_{t=t_i}^{2t_m} P_n(t)/N_{(2t_m-t_i)}}{4} \tag{24}$$

$$F_{av} = \frac{\sum_{t=0}^{t_s} F_g(t)/N_{t_s} + \sum_{t=t_s}^{t_i} F_s(t)/N_{(t-t_t)}}{4} + \frac{F_r + \sum_{t=t_i}^{2t_m} F_p/N_{(2t_m-t_t)}}{4} \tag{25}$$

where $N_{t_s}, N_{(t_i-t_s)}, N_{(2t_m-t_i)}$ are the numbers of discrete points in each phase.

4) ENERGY DISSIPATION THROUGHOUT THE CONTACT PHASE

The energy dissipation values for four contact phases of solid-solid interface in macroscopic relative motion are as follows:

$$\begin{aligned} D_g &= \int_0^{\xi_g} F_g d\xi = \int_0^{Vt} F_g d\xi, \ 0 \le t < t_s \\ D_{si} &= \int_{\xi_g}^{\xi_{si}} (F_{si} - F_g) d\xi = \int_0^{Vt} (F_{si} - F_g) d\xi, \ t_s \le t \le t_i \\ D_p &= \int_{\xi_{si}}^{\xi_p} |F_p - F_{si}| d\xi = \int_0^{Vt} |F_p - F_{si}| d\xi, \ t_i \le t \le 2t_m \end{aligned} \tag{26}$$

B. CALCULATION OF TANGENTIAL CONTACT STIFFNESS AND DAMPING OF SOLID-SOLID INTERFACE IN MACROSCOPIC RELATIVE MOTION

Suppose the height of the asperity is z, the height of the asperity on the rough surface obeys the Gaussian distribution, the function is $\phi(z)$, the density of the asperity is η_n, and suppose A is the nominal contact area of the joint surface, d is the normal distance between the ideal rigid plane and the average height surface of the asperity, and δ is the normal deformation of the asperity under normal load, then $z = \delta + d$. Using the statistical theory, when the above contact characteristic parameter model of a single asperity is extended to the whole solid interface, the total contact stiffness $K_{\tau s}$ of the contact surface is:

$$K_{\tau s} = A\eta_n \int_d^{d+\delta} \left[\frac{\sum_{t=0}^{t_s} K_g/N_{t_s} + \sum_{t=t_s}^{t_i} K_s/N_{(t_i-t_s)}}{4} \cdots + \frac{K_r + \sum_{t=t_i}^{2t_m} K_p/N_{(2t_m-t_i)}}{4} \right] \phi(z) dz \tag{27}$$

Using Equations (15), (18), (20) and (23) to calculate K_g, K_s, K_r, K_p, and substituting them into Equation (27), $K_{\tau s}$ can be obtained.

It is assumed that the total energy dissipation of the contact surface is $D_{\tau s}$, which is the sum of the energy dissipation of each contact phase (growth phase, stagnation phase, crack phase and propagation phase), as shown in Equation (28):

$$D_{\tau s} = A\eta_n \int_d^{d+\delta} (D_g + D_{si} + D_p)\phi(z)dz \tag{28}$$

Since the work done by the viscous damping force is equal to the product of the damping force and the moving displacement and is equal to the energy consumed by it, the total equivalent viscous damping energy consumption E_C is:

$$E_C = C_{\tau s}V^2 t, \quad 0 \le t \le 2t_m \tag{29}$$

where $C_{\tau s}$ is the equivalent viscous damping coefficient. The total contact friction energy consumption of each contact phase is equivalent to viscous damping energy consumption, that is, if Equation (28) is equal to Equation (29), then

$$C_{\tau s} = \frac{D_{\tau s}}{2V^2 t_m} \tag{30}$$

Substituting Equation (28) into it, the results will be obtain.

The total normal contact load of macroscopic relative motion solid-solid interface is:

$$P_{nsum} = A\eta_n \int_d^{d+\delta} P_{av}\phi(z)dz \tag{31}$$

The total tangential friction force of macroscopic relative motion solid-solid interface is:

$$F_{sum} = A\eta_n \int_d^{d+\delta} F_{av}\phi(z)dz \tag{32}$$

The friction coefficient of macroscopic relative motion solid-solid interface is

$$f_{sum} = \frac{F_{sum}}{P_{nsum}} \tag{33}$$

III. TANGENTIAL STIFFNESS AND DAMPING MODEL OF SOLID-LIQUID INTERFACE IN MACROSCOPIC RELATIVE MOTION

The calculation of tangential contact characteristics of solid-liquid interface can be reduced to the solution of tangential contact stiffness and damping of solid and fluid. The calculation of fluid tangential contact stiffness and damping starts with the average flow equation considering roughness lubrication effect, and the oil film pressure distribution, film thickness distribution, oil film bearing capacity and tangential viscous shear force of oil film are obtained, and then the tangential stiffness and damping of oil film are obtained. It is assumed that the lubricating oil in the macroscopic relativemotion joint is in t The calculation of tangential contact characteristics of solid-liquid interface can be reduced to the solution of tangential contact stiffness and damping of solid and fluid. The calculation of fluid tangential contact stiffness and damping starts with the average flow equation considering roughness lubrication effect, and the oil film pressure distribution, film thickness distribution, oil film bearing capacity and tangential viscous shear force of oil film are obtained, and then the tangential stiffness and damping of oil film are obtained. It is assumed that the lubricating oil in the macroscopic relative motion joint is in the state of mixed lubrication, and the thermal effect in the lubricating oil is not considered, and it is isothermal.

A. FLUID CONTACT MODEL OF SOLID-LIQUID INTERFACE IN MACROSCOPIC RELATIVE MOTION

1) REYNOLDS EQUATION CONSIDERING ROUGHNESS LUBRICATION EFFECT

For the macroscopic relative motion solid-liquid interface in the state of mixed lubrication, it is necessary to consider the effect of surface roughness on the lubrication effect. Using the Reynolds Equation established by Wu et al. [44]:

$$\frac{\partial}{\partial x}\left(\frac{h_r^3}{\eta_f}\phi_x\frac{\partial \overline{p_f}}{\partial x}\right) + \frac{\partial}{\partial y}\left(\frac{h_r^3}{\eta_f}\phi_y\frac{\partial p}{\partial y}\right) = 6U\left[\phi_c\frac{\partial h_r}{\partial x} + \sigma\frac{\partial \phi_s}{\partial x}\right] + 12\phi_c\frac{\partial h_r}{\partial t} \tag{34}$$

where $\overline{p_f}$ is the average oil film pressure; h_r is the nominal oil film thickness of each point; σ is the comprehensive roughness of two rough surfaces; ϕ_x and ϕ_y are the pressure flow factor along the x and y directions, ϕ_s is the pressure flow factor, ϕ_c is the contact probability factor, and their values are calculated by the empirical fitting equation in [27]; U stands for the relative sliding velocity of the two surfaces in the X direction, that is V; η_f is the viscosity of lubricating oil, which is calculated using Reoland's Viscosity-Pressure Relation in [45] in Equation (35).

$$\eta_f = \eta_0 exp\left\{(\ln\eta_0 + 9.67)\left[-1 + (1 + \frac{p}{p_0})^2\right]\right\} \tag{35}$$

where η_f is the viscosity under pressure p; η_0 is the viscosity under atmospheric pressure; p_0 is the pressure coefficient, preferably 5.1×10^{-9}; and for general mineral oils, z is usually 0.68.

In the actual working condition, the relative moving surface is not completely parallel, and the thickness of the lubricating oil film changes continuously in the whole contact lubrication area during the sliding process. For example, when the sliding guide of the machine tool moves relatively, the experiment shows that [46], a wedge-shaped oil film with an inclination angle α will be formed between the two surfaces, as shown in Figure 5.

Therefore, according to the geometric size of the slider with a length of 2d and a width of b, the nominal film thickness h_r can be expressed as follows:

$$h_r(x) = h_0 + \alpha x \tag{36}$$

where the inclination angle $\alpha = (h_1 - h_0)/d$. The equation of film thickness differs between two rough surfaces with different characteristics, that is, Equation (36) takes different forms.

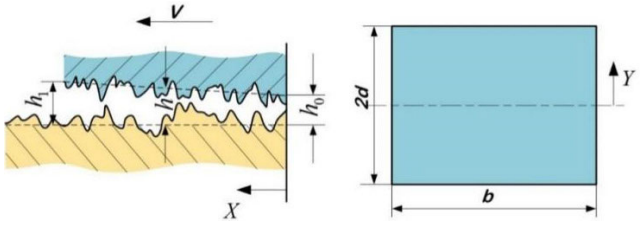

FIGURE 5. Contact of a lubricating rough surface with finite length in relative motion.

Due to the existence of different degrees of surface roughness of processed parts, the true oil film thickness h_T between the bonding surfaces can be expressed as:

$$h_T(x, y) = h_0(x, y) + \delta_1(x, y) + \delta_2(x, y) \tag{37}$$

where h_0 indicates the minimum oil film thickness between the two rough surfaces; δ_1 and δ_2 represent the roughness amplitudes of upper and lower rough surfaces, respectively.

The common methods for solving Reynolds equation (34) include: finite difference method, multigrid method and finite element method. The finite difference method is one of the earliest and mature numerical analysis methods, which is selected in this article.

Dimensionless treatment of Reynold's equation are dealt with:

$$T = t/t_0,\ H = h_r/h_0;\ P = \overline{p_f}/p_0;\ X = x/L;\ Y = y/L;$$
$$\psi_1 = \frac{6U\eta_f L}{h_0^2 p_0};\ \psi_2 = \frac{6U\eta_f L\sigma}{h_0^3 p_0};\ \psi_3 = \frac{12\eta_f L}{h_0^2 p_0}$$

The average Reynold's equation after dimensionless treatment is:

$$\frac{\partial}{\partial X}(\phi_x H^3 \frac{\partial P}{\partial X}) + \frac{\partial}{\partial Y}(\phi_y H^3 \frac{\partial P}{\partial Y}) = \psi_2 \frac{\partial \phi_c}{\partial X} + \psi_1 \phi_s \frac{\partial H}{\partial X} + \psi_3 \frac{\partial \phi_c}{\partial T}. \tag{38}$$

In order to facilitate the calculation and solution, the difference form of Equation (38) can be obtained using the finite difference method:

$$A(i,j)P(i,j) - B(i,j)P(i-1,j) - C(i,j)P(i+1,j) - D(i,j)P(i,j-1) - E(i,j)P(i,j)P(i,j) = F(i,j) \tag{39}$$

where

$$B(i,j) = \frac{\left[\phi_x(i-1,j)H^3(i-1,j) + \phi_x(i,j)H^3(i,j)\right]}{2\Delta X^2}$$
$$C(i,j) = \frac{\left[\phi_x(i+1,j)H^3(i+1,j) + \phi_x(i,j)H^3(i,j)\right]}{2\Delta X^2}$$
$$D(i,j) = \frac{\left[\phi_y(i,j-1)H^3(i,j-1) + \phi_y(i,j)H^3(i,j)\right]}{2\Delta Y^2}$$
$$E(i,j) = \frac{\left[\phi_y(i,j+1)H^3(i,j+1) + \phi_y(i,j)H^3(i,j)\right]}{2\Delta Y^2}$$
$$A(i,j) = B(i,j) + C(i,j) + D(i,j) + E(i,j)$$
$$F(i,j) = \frac{\psi_2}{2\Delta X}\left[\phi_c(i+1,j) - \phi_c(i-1,j)\right] + \frac{\psi_1}{2\Delta X}\phi_s(i,j) \times \left[H(i+1,j) - H(i-1,j)\right] + \frac{\psi_3}{2\Delta T}\left[\phi_c(i+1,j) - \phi_c(i-1,j)\right] \tag{40}$$

Therefore,

$$P^{k+1}(i,j) = \kappa * G + (1-\kappa) * P^k(i,j) \tag{41}$$

where κ is the relaxation factor. According to the calculation experience, the overrelaxation iteration is adopted, preferably $\kappa = 0.95$,

$$G = \frac{\begin{bmatrix} B(i,j)P^k(i-1,j) + C(i,j)P^k(i+1,j) \\ +D(i,j)P^k(i,j-1) + E(i,j)P^k(i,j+1) \end{bmatrix} + F(i,j)}{A(i,j)}$$

2) CALCULATION OF BEARING CAPACITY OF OIL FILM

The contact pressure of solid-liquid interface consists of two parts, one is the bearing capacity caused by asperity contact, and the other is the bearing capacity of oil film produced by hydrodynamic pressure under mixed lubrication [47]. The bearing capacity Q_1 of oil film on surface of length L and width W and is:

$$Q_1 = \int_0^W \int_0^L \bar{p}_y dxdy \tag{42}$$

The bearing capacity Q_2 of asperity is:

$$Q_2 = \int_0^W \int_0^L P_{nsum} dxdy \tag{43}$$

The total bearing capacity Q_0 is:

$$Q_0 = Q_1 + Q_2 \tag{44}$$

3) OIL FILM PRESSURE DISTRIBUTION AND FILM THICKNESS DISTRIBUTION

The solution process of oil film pressure and film thickness is shown in Figure 6.

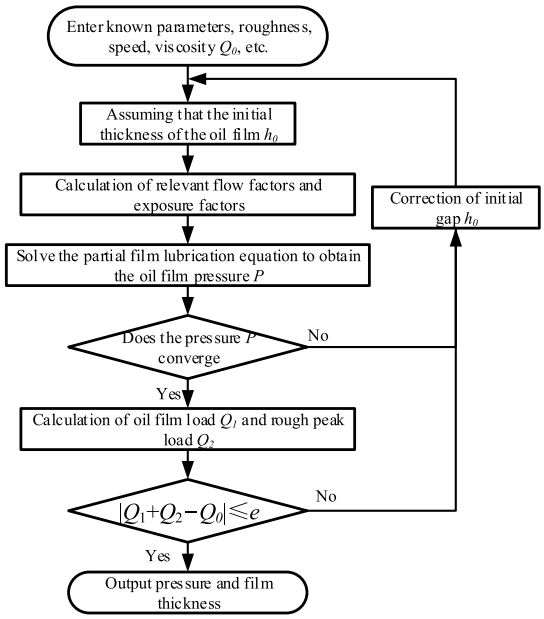

FIGURE 6. Solution flow of oil film pressure distribution and film thickness distribution.

When solving the problem, the known material parameters, the number of nodes and the initial values of the parameters such as moving velocity, lubricating oil viscosity and oil film thickness are given, and the film thickness of each node is calculated according to Equation (36). Thus, the film thickness ratio of each node is obtained, and the flow factor and contact factor under each node are calculated according to the film thickness ratio. The partial film lubrication equation is solved by the relaxation iterative method of Equation (41), the oil film pressure under each node is obtained, the partial bearing capacity of the oil film is calculated according to the Equation (42), and the bearing capacity of the solid part is calculated according to the Equation (43). Judge whether the difference between the sum of the partial bearing capacity of the oil film and the solid part and the set load value is less than the given tolerance value, if not. The solid bearing capacity and the oil film bearing capacity are updated by adjusting the oil film thickness until the error is less than the given tolerance value, and finally the result is output.

4) CALCULATION OF VISCOUS SHEAR FORCE OF OIL FILM

The viscous shear force of oil film is calculated based on the model proposed by Patir and Cheng [48].

$$F_f = -\int_0^W \int_0^L \left[\frac{\eta_f U}{h_r}(\phi_f + \phi_{fs})\right] dxdy \tag{45}$$

where ϕ_f and ϕ_{fs} are shear stress factors, and their numerical calculation equations can be found in [45].

5) CALCULATION OF TANGENTIAL STIFFNESS AND DAMPING OF OIL FILM

The tangential stiffness of the oil film on the solid-liquid interface in macroscopic relative motion is calculated by the small disturbance method, and the tangential damping is calculated by the derivation of the oil film shear force. The oil film stiffness and damping at each moment ($t \in [0, T]$) are as follows:

$$\begin{cases} K_{\tau f}^{(t)} = k_\tau = \dfrac{\Delta F_f}{\Delta x} = \dfrac{F'_{fd} - F_{fd}}{\Delta x} \\ C_{\tau f}^{(t)} = c_\tau = \dfrac{\partial F_f}{\partial U} = \dfrac{\eta_f^{(t)}}{h_r^{(t)}}(\phi_f^{(t)} + \phi_{fs}^{(t)}) \end{cases} \tag{46}$$

where k_τ is the tangential stiffness of the oil film, c_τ is the tangential damping of the oil film, Δx is the tangential displacement, the value is $V\Delta t$, ΔF_f is the change of the viscous shear force of the oil film caused by the displacement disturbance, and $F_{fd}{}'$, F_{fd} are the transient viscous shear forces caused by the displacement disturbance at the previous time and the current moment, obtained by Equation (45). $\eta_f^{(t)}$, $h_r^{(t)}$, $\phi_f^{(t)}$, $\phi_{fs}^{(t)}$ are the viscosity, thickness and shear factor of oil film at the current time.

The average contact stiffness and damping of the oil film in the four contact phases is

$$\begin{cases} \bar{K}_{\tau f} = \dfrac{1}{2t_m}\sum_0^{2t_m} K_{\tau f}^{(t)} \\ \bar{C}_{\tau f} = \dfrac{1}{2t_m}\sum_0^{2t_m} C_{\tau f}^{(t)} \end{cases} \tag{47}$$

B. FRICTION COEFFICIENT OF SOLID-LIQUID INTERFACE IN MACROSCOPIC RELATIVE MOTION

The total friction force F of solid-liquid interface is the sum of the viscous shear force of oil film and the friction force of solid part.

$$F = -\int_0^W \int_0^L \left[\frac{\eta_f U}{h_r}(\phi_f + \phi_{fs}) + F_{sum}\right] dxdy \tag{48}$$

Then, it is only necessary to substitute Equation (32) into it.

Therefore, the friction coefficient f of the solid-liquid interface in macroscopic relative motion is

$$f = \frac{F}{Q_0} \tag{49}$$

Then, it is only necessary to substitute Equation (44), i.e. the total bearing capacity of solid-liquid interface, into it.

C. CALCULATION MODEL OF TANGENTIAL CONTACT STIFFNESS AND DAMPING OF SOLID-LIQUID INTERFACE IN MACROSCOPIC RELATIVE MOTION

From theoretical analysis and experimental demonstration in [23], [26] and [49], it can be seen that the total tangential contact stiffness of the relative motion solid-liquid interface is the sum of the solid contact stiffness and the oil film tangential stiffness, and the total tangential damping is the sum of the solid contact damping and the oil film tangential damping. The tangential contact stiffness of solid-liquid interface is obtained from Equations (27) and (47).

$$K_{sum} = K_{\tau s} + \overline{K}_{\tau f} \tag{50}$$

From Equations (30) and (47), the tangential equivalent viscous damping coefficient of solid-liquid interface can be obtained as follows:

$$C_{sum} = C_{\tau s} + \overline{C_{\tau f}} \tag{51}$$

IV. SIMULATION ANALYSIS OF TANGENTIAL CONTACT MODEL OF SOLID-LIQUID INTERFACE WITH MACROSCOPIC RELATIVE MOTION

The changes of normal contact load and moving velocity will affect the contact parameters of the solid part and the fluid part, and then affect the tangential contact stiffness and damping of the relatively moving solid-liquid interface. In order to reveal the influence law of various factors,

the numerical simulation is carried out by using MATLAB software.

The parameters in the model are dimensionless with reference to [26], and represented by the symbol "$*$".

The mechanical parameters of the surface are selected as $E_1 = E_2 = 2.07 \times 10^{11}$ Pa, Poisson's ratio $\nu_1 = \nu_2 = 0.29$, $H = 1.96$ GPa, material's yield strength $p_y = 18$ GPa, standard deviation of height distribution of rough surface $\sigma = 1.89 \times 10^{-6}$, radius of curvature $R_1 = R_2 = 1.00 \times 10^{-6}$m, shear modulus in the elastic phase $G_r = 1.403 \times 10^{-14}$, nominal contact area $A = 7.07 \times 10^{-4}$ m^2, lubricating oil viscosity $\eta = 80$ mm^2/s, oil film inclination $\alpha = 0.02$, joint surface length l=1e−3 m, width w=1e−3 m. The parameters in the asperity contact model are selected in [39], preferably, $n = 0.25$, $I_r = 3.9$, $k_s = 0.26$, $\varepsilon\tau_B = 0.175 \times 10^{-11}$, the moving velocity $V^* = \frac{V}{V_r} = 1$, $V_r^* = 1$. Time parameters, compared with t_0, are given dimensionless processing, preferably $t_s^* = 0.011$, $t_m^* = 0.043$, $t_i^* = 0.045$, $t_0^* = 1$, and $t_0^* = 2.52$.

A. VARIATION OF TANGENTIAL FORCE AND NORMAL LOAD OF ASPERITY WITH TIME IN DIFFERENT PHASES OF SOLID CONTACT

The analysis of the variation law of tangential force and normal load of a pair of asperities at different phases of contact is helpful to reveal the mechanism and essence of solid contact microscopically. As shown in Figure 7 (a), (b), (c) and (d), the tangential friction and normal load of the asperity change with time at each contact phase. It can be seen from Figure 7 (a), (b) and (c) that in the growth phase, the tangential force of the asperity increases nonlinearly with the increase of time, this is due to the fact that with the sliding, the two asperities contact each other and gradually embed into each other's surface, forming a bonding area, and the contact area is increasing. In the stagnation phase, the sliding contact stagnates, but the bonding area formed between the two asperities is not destroyed, the contact area further increases, and the tangential force at the boundary of the contact area begins to increase rapidly, and then the increase of the contact area slows down. The nonlinear increase of tangential force becomes slow, followed by a short crack adhesion phase, where the crack appeared in the contact bonding zone, the sliding continued, the crack gradually expanded and propagated, the two asperities gradually separated, the contact area began to decrease, and the tangential force of the asperity gradually decreased until the end of the contact. As is shown in Figure 7 (d), during the whole contact phase, the normal contact load of the asperity changes in the same way as the contact area, which first increases and then decreases nonlinearly.

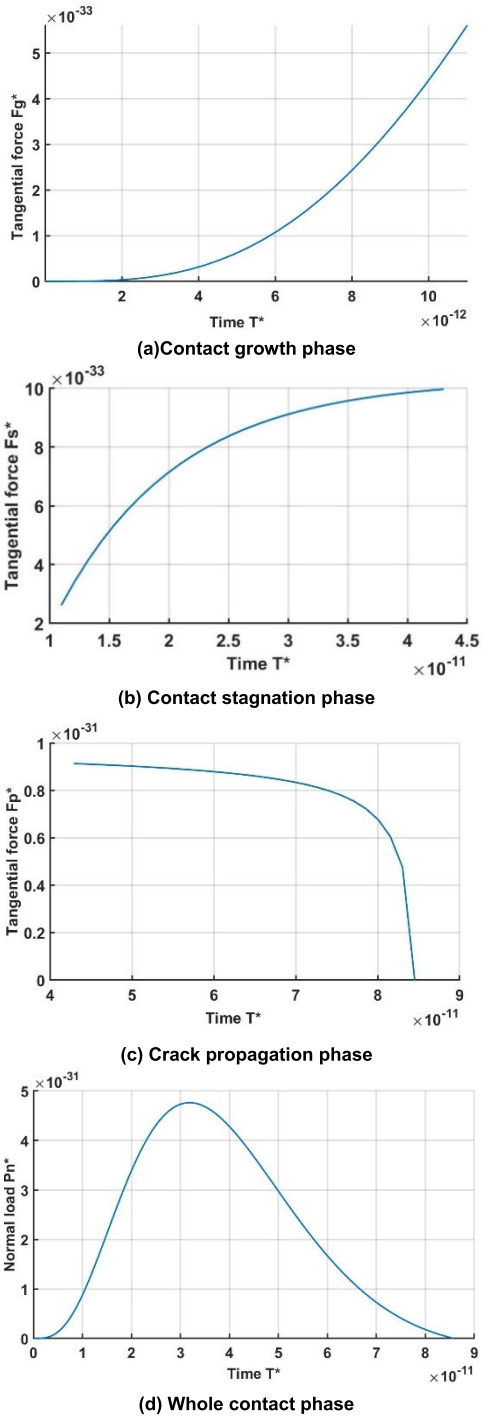

FIGURE 7. Variation of tangential contact force and normal load with time in each period.

B. SIMULATION ANALYSIS OF OIL FILM PRESSURE DISTRIBUTION AND FILM THICKNESS DISTRIBUTION ON SOLID-LIQUID INTERFACE IN MACRO RELATIVE MOTION

In the state of mixed lubrication, the relative motion of solid-liquid interface contact, solid contact and oil film contact coexist. By simulating the distribution characteristics of oil film pressure and film thickness, the degree of solid and oil film contact can be analyzed. Figure 8 shows the oil film pressure distribution and oil film thickness distribution under normal load. Because the oil film thickness equation is a wedge-shaped oil film formed by the sliding guide, the oil film thickness is distributed in an oblique plane. The oil film pressure shows a parabola shape which first increases and

then decreases along the X and Y directions, and the value is zero at the boundary.

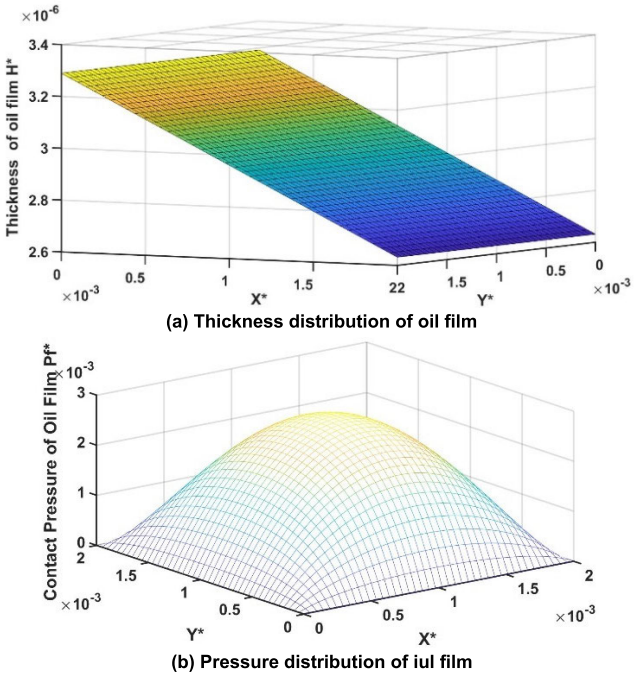

FIGURE 8. Thickness and pressure distributions of oil film under load $P_n^* = 4.42e-7$.

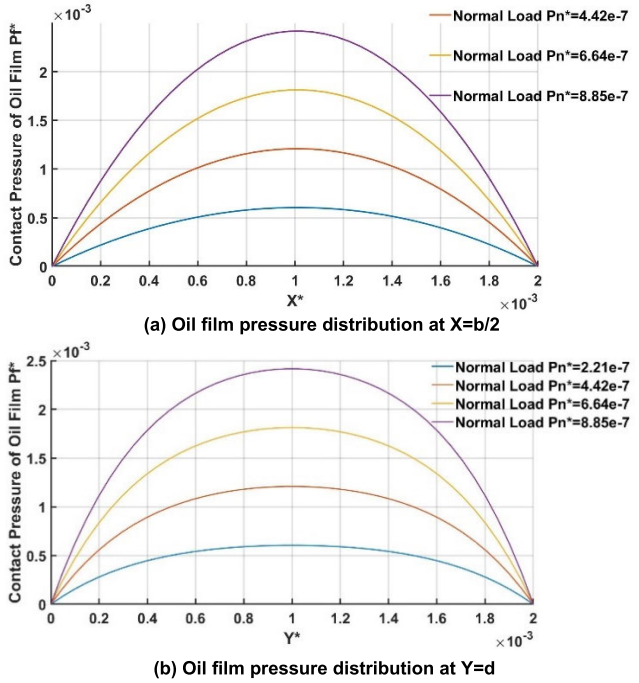

FIGURE 9. Oil film pressure distribution under different loads.

As shown in Figure 9, the oil film pressure distribution at the central section of the sliding rail slider in the X and Y directions under different normal loads at the moving velocity $V^* = 1$. It can be seen from the figure that the oil film pressure first increases and then decreases along the X direction and Y direction, and the greater the normal load, the greater the oil film pressure. This is due to the increase of the normal load, the increase of the number of contact asperities, the decrease of the oil film load ratio, but the increase of the total oil film pressure. It can be seen from Figure 9(a) that the oil film pressure in the X direction is asymmetrically distributed due to the influence of the oil film inclination angle α. Because the oil film inclination angle here is small, the skew degree of the pressure distribution is not obvious. It can be seen from Figure 9 (b) that the oil film pressure in the Y direction shows a symmetrical parabolic distribution because the oil film thickness is the same at the same Y value.

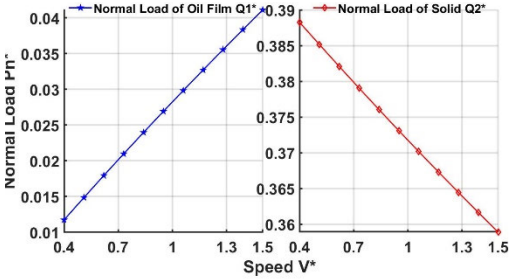

FIGURE 10. Effect of moving velocity on bearing capacities of oil film and solid.

The effect of moving velocity on the bearing capacity of oil film and solid is shown in Figure 10. It can be seen from the figure that with the increase of velocity, the bearing capacity of oil film increases almost linearly, while the bearing capacity of asperity decreases.

From the numerical point of view, the asperity contact is still the main body in the solid-liquid interface, and the proportion of oil film contact is very small. But microscopically, the residual lubricating oil in the gully formed by the asperities on the surface will occur the phenomenon of hydrodynamic lubrication at the asperity level when the moving velocity increases, which improves the bearing capacity of the lubricating oil film.

Figure 10 shows the effect of moving speed on the bearing capacity of oil film and solid. It can be seen from the figure that with the increase of speed, the bearing capacity of oil film increases almost linearly, while the bearing capacity of asperity decreases. From the numerical point of view, the micro-convex contact is still the main body in the solid-liquid interface, and the proportion of oil film contact is very small. But microscopically, the residual lubricating oil in the gully formed by the asperity on the surface will occur the phenomenon of hydrodynamic lubrication at the micro level when the moving speed increases, which improves the bearing capacity of the lubricating oil film.

C. SIMULATION ANALYSIS OF FRICTION COEFFICIENT OF SOLID-LIQUID INTERFACE WITH MACROSCOPIC RELATIVE MOTION

Figure 11 shows the relationship between the friction coefficient of the solid-liquid interface and the normal load. With the increase of normal contact load, the friction

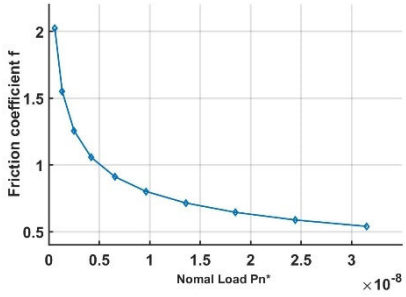

FIGURE 11. Relationship between friction coefficient and normal load of solid-liquid interface.

coefficient of the solid-liquid interface decreases, and the curve is consistent with the curve obtained by experiment in [50] and [51]. When the normal load increases, the number of contact asperity increases, the proportion of solid load increases, the fluid action weakens, and solid-solid contact gradually occupies a dominant position. When the rough surface slides macroscopically, the sliding resistance increases with the increase of normal load, but the increasing rate is less than that of normal load, so the friction coefficient decreases with the increase of normal load. In addition, with the relative sliding of the joint surface, the residual part of the lubricating oil in the micro-convex gully will form a microscopic hydrodynamic lubrication effect at the edge, and the lubricating oil will be drawn out from the micro-convex gully and spread to the contact area of the micro-convex body. The friction performance of the contact surface is further improved, that is, the friction coefficient is reduced.

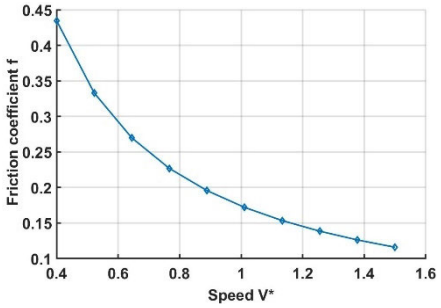

FIGURE 12. Relationship between friction coefficient and moving speed of solid-liquid interface.

It can be seen from Figure 12 that the friction coefficient of solid-liquid interface decreases nonlinearly with the increase of velocity. The curve is consistent with the curve obtained by experiment in [50] and [51]. With the increase of the moving speed, the hydrodynamic pressure effect becomes stronger and stronger, which makes the thickness of the lubricating oil film and the average distance between the contact surface become larger and larger, and the contact deformation of the micro-convex body on the rough surface decreases gradually. at this time, the fluid load increases gradually, the solid load gradually weakens, and the fluid contact is dominant, but it is still in the state of mixed lubrication. According to the Stribeck effect, the friction coefficient decreases with the increase of moving speed.Therefore, the friction coefficient decreases with the increase of moving speed.

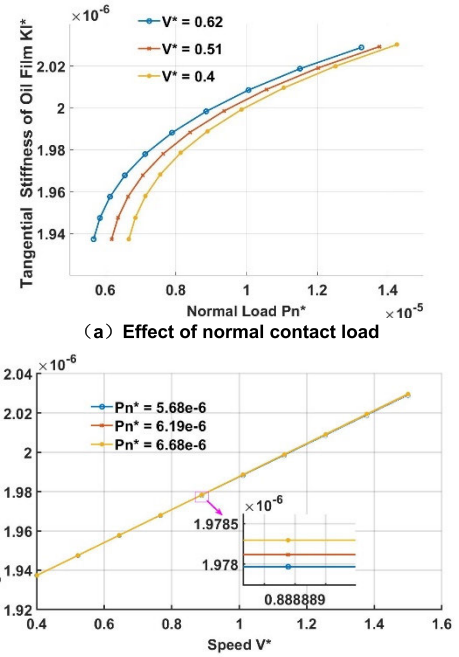

(a) Effect of normal contact load

(b) Effect of moving velocity

FIGURE 13. Effects of normal contact load and moving velocity on oil film tangential contact stiffness.

D. SIMULATION ANALYSIS OF TANGENTIAL STIFFNESS OF SOLID-LIQUID INTERFACE WITH MACROSCOPIC RELATIVE MOTION

1) EFFECT OF NORMAL CONTACT LOAD AND MOVING VELOCITY ON OIL FILM TANGENTIAL CONTACT STIFFNESS

Figures 13 (a) and (b) show the variation of tangential shear stiffness of oil film with normal load and moving velocity. It can be seen from the diagram that the tangential contact stiffness of oil film increases nonlinearly with the increase of normal load. This is because with the increase of normal contact load, according to Equation (33), the viscosity of lubricating oil increases, the ability of oil film to resist deformation in tangential direction increases, so the tangential stiffness increases. With the increase of the moving velocity, the tangential stiffness of the oil film increases almost linearly, because the increase of the moving velocity will increase the shear rate of the oil film, thus the tangential stiffness increases. The variation of tangential shear stiffness of oil film at normal load and moving velocity is consistent with the results of [24] and [25].

2) COMPARISON OF TANGENTIAL CONTACT STIFFNESS BETWEEN SOLID-SOLID INTERFACE AND SOLID-LIQUID INTERFACE IN MACROSCOPIC RELATIVE MOTION

Figures 14 (a) and (b) compare the tangential contact stiffness of solid-solid interface and solid-liquid interface

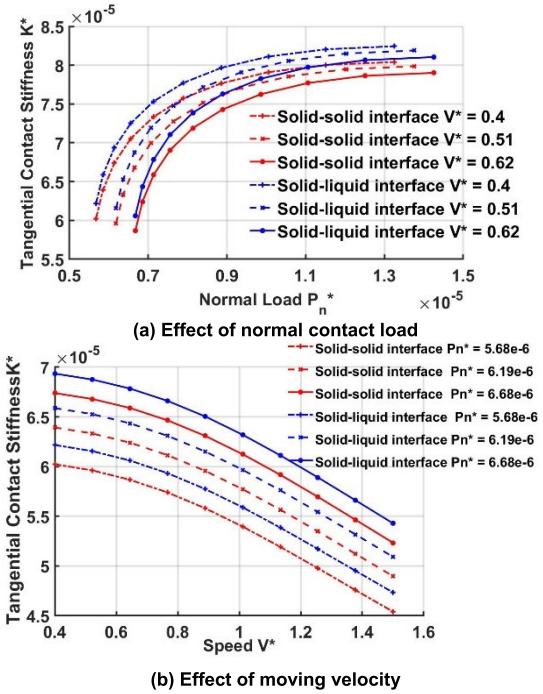

FIGURE 14. Tangential contact stiffness contrast between solid-solid interface and solid-liquid interface in relative motion.

with normal contact load and moving velocity. It can be seen from Figure 14 (a) that with the increase of normal contact load, the contact stiffness of solid-liquid interface and solid-solid interface increases nonlinearly, and then the increase becomes smooth. This is because with the increase of normal contact load, the actual contact area between asperities increases, and the number of contact asperities increases, thus the ability to resist tangential displacement is enhanced, that is, the tangential stiffness of solid-solid interface increases, but to a certain extent, the actual contact area between asperities and the number of contact asperities almost reach the maximum, this effect becomes smaller and smaller, and the trend slows down, which conforms with the results from [52] and [53]. For the solid-liquid interface, due to the increase of the oil film stiffness, the oil film stiffness is one order of magnitude smaller than that of the solid-solid interface, and the influence is limited. As a result, the tangential contact stiffness of the solid-liquid interface is the same as that of the solid-solid interface, and the value is always slightly higher. It can be seen from Figure 14 (b) that the tangential contact stiffness of solid-liquid interface and solid-solid interface decreases nonlinearly with the increase of moving velocity. This is because the larger the moving velocity is, the smaller the friction coefficient of the solid-solid interface [54]. When the normal load is constant, the tangential friction force decreases, and the tangential displacement increases with the increase of the moving velocity, so the tangential contact stiffness of the solid-solid interface decreases., this variation law is consistent with the results from [55]. As can be seen from Figure 13(b), the stiffness of the oil film increases with the increases of the moving velocity, but it is an order of magnitude smaller than that of the solid-solid interface, the solid-solid contact is still dominant, and the influence of the oil film is limited, so the solid-liquid interface shows the same trend as the solid-solid interface, and the numerical value is always slightly higher.

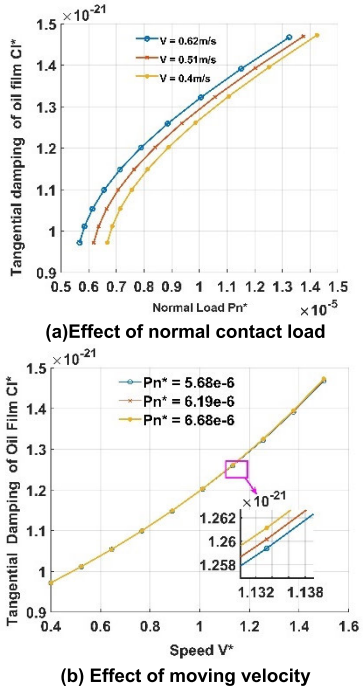

FIGURE 15. Effects of normal contact load and moving velocity on oil film tangential contact damping.

E. SIMULATION ANALYSIS OF TANGENTIAL CONTACT DAMPING OF SOLID-LIQUID INTERFACE IN MACROSCOPIC RELATIVE MOTION

1) EFFECT OF NORMAL CONTACT LOAD AND MOVING VELOCITY ON OIL FILM TANGENTIAL CONTACT STIFFNESS

Figures 15(a) and (b) indicate the variation of tangential damping coefficient of relative motion oil film with normal load and moving velocity. It can be seen from the diagram that the tangential damping coefficient of oil film increases nonlinearly with the increase of normal contact load, for with the increase of normal contact load, the viscosity of lubricating oil increases, the friction energy consumption increases, so that the tangential damping coefficient increases; and that with the increase of moving velocity, the tangential damping coefficient of oil film increases nonlinearly, in that the increase of moving velocity will increase the shear rate of oil film and the energy consumption of tangential shear resistance, so that the tangential damping coefficient increases. The variation of tangential damping coefficient of oil film at normal load and moving velocity is consistent with the results of [24] and [25].

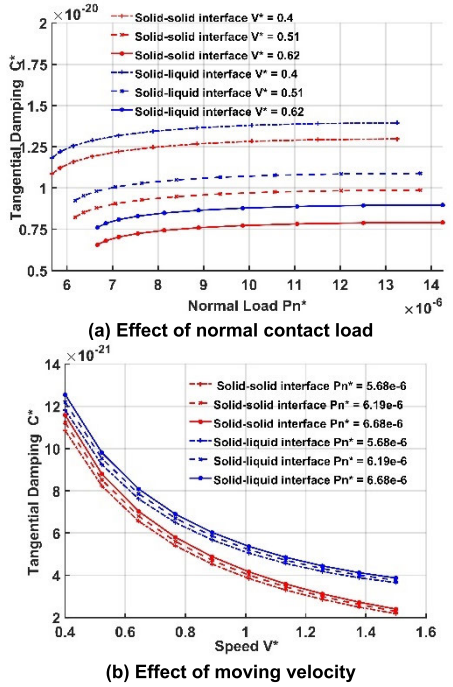

FIGURE 16. Comparison of tangential contact damping between solid-solid interface and solid-liquid interface in relative motion.

2) COMPARISON OF TANGENTIAL CONTACT DAMPING BETWEEN SOLID-SOLID INTERFACE AND SOLID-LIQUID INTERFACE IN RELATIVE MOTION

Figures 16 (a) and (b) illustrate the variation of tangential damping coefficients of solid-solid interface and solid-liquid interface with normal contact load and moving velocity. It can be seen from the diagram that the tangential contact damping coefficients of solid-liquid interface and solid-solid interface increase slowly and nonlinearly with the increase of normal contact load. For the solid-solid interface, with the increase of the normal contact load, the actual contact area between the asperities increases, the number of contact asperities increases, the tangential friction energy dissipation increases, so the tangential damping coefficient increases. For the solid-liquid interface, although the effect of oil film damping is increased, the oil film damping is one order of magnitude smaller than the solid-solid interface damping, and the effect is limited. As a result, the tangential contact damping of the solid-liquid interface varies with the normal load, and the value is always slightly higher. With the increase of moving velocity, the tangential contact stiffness of solid-liquid interface and solid-solid interface decreases nonlinearly. This is because the This is because the greater the moving velocity, the smaller the friction coefficient of the solid-solid interface [54]. When the normal load is constant, the smaller the tangential friction force is, the smaller the friction energy consumption is, and the tangential displacement increases with the increase of velocity. It can be seen from equation (28), the damping coefficient of solid-solid interface decreases rapidly. Although the damping of oil film increases with the increase of moving velocity, the damping of oil film is one order of magnitude smaller than that of solid-solid interface, and the effect is limited, so the change trend of solid-liquid interface is the same as that of solid-solid interface, and the value is always slightly higher.

V. CONCLUSION

In this article, aiming at the lack of tangential contact modeling of macroscopic relative motion solid-liquid interface considering the interaction between lubricating oil and rough surface, based on the sliding friction adhesion model of Savkoor single pair of asperity, the tangential contact models of solid part and fluid part of macroscopic relative motion solid-liquid interface are established respectively, and the tangential contact stiffness and damping models of solid-liquid interface are proposed. The law of variation with normal load and moving velocity is simulated. The results show that: (1) the contact characteristics of solid-liquid interface and solid-solid interface are similar, and the tangential contact stiffness and damping of solid-liquid interface are always larger than those of solid-solid interface, which shows that the macroscopic relative motion interface of oil-bearing medium has good stiffness and damping characteristics, which is more suitable for mechanical equipment. (2) the tangential contact stiffness and damping of solid-liquid interface increase nonlinearly with the increase of normal contact load and decrease nonlinearly with the increase of moving velocity. Therefore, the low velocity and heavy load conditions can improve the tangential stiffness and damping of the equipment.

REFERENCES

[1] Z. Wang, W. Pu, X. Pei, and W. Cao, "Contact stiffness and damping of spiral bevel gears under transient mixed lubrication conditions," *Friction*, vol. 10, no. 4, pp. 545–559, Apr. 2022.

[2] L. L. Liu, H. Z. Liu, and Z. Y. Wu, "Modeling and analysis of machine tool feed servo system with friction and backlash," *Trans. Chin. Soc. Agricult. Machinery*, vol. 41, no. 11, pp. 212–218, 2010.

[3] C. Rebelein, J. Vlacil, and M. F. Zaeh, "Modeling of the dynamic behavior of machine tools: Influences of damping, friction, control and motion," *Prod. Eng.*, vol. 11, no. 1, pp. 61–74, Feb. 2017.

[4] M. Yin, W. T. Cheng, L. J. Bai, and L. L. Guo, "Numerical control machine tool motion simulation and analysis of parts of the crawling phenomenon," *Adv. Mater. Res.*, vols. 971–973, pp. 592–595, Jun. 2014.

[5] Z. Zhao, J. Niu, Y. Shen, and S. Yang, "Forced vibration of two-degrees-of-freedom machine tool feed system with clearance and friction," *Appl. Math. Model.*, vol. 92, pp. 281–296, Apr. 2021.

[6] J. Z. Hu, M. Wang, X. S. Gao, and T. Zan, "Axial contact stiffness analysis of position preloaded ball screw mechanism," *J. Mech. Eng.*, vol. 50, no. 7, pp. 60–69, 2014.

[7] M. K. Huang, "Analysis and dynamic simulation of creep mechanism in machine tool feed system," M.S. thesis, Nanjing Univ. Aeronaut. Astronaut., Nanjing, China, 2019.

[8] R. Sato, S. Noguchi, T. Hokazono, I. Nishida, and K. Shirase, "Time domain coupled simulation of machine tool dynamics and cutting forces considering the influences of nonlinear friction characteristics and process damping," *Precis. Eng.*, vol. 61, pp. 103–109, Jan. 2020.

[9] W. Li, "Analysis of elastic-plastic contact friction and wear on rough contact surfaces and study of energy dissipation," M.S. thesis, South China Univ. Technol., Guangzhou, China, 2021.

[10] M. Eriten, S. Chen, A. D. Usta, and K. Yerrapragada, "In situ investigation of load-dependent nonlinearities in tangential stiffness and damping of spherical contacts," *J. Tribol.*, vol. 143, no. 6, pp. 1–11, Jun. 2021.

[11] Z. Q. Gao, "Research of theoretical model on contact stiffness and damping for the mechanical joint surface," Ph.D. dissertation, Xi'an Univ. Technol., Xi'an, China, 2018.
[12] X. Zhang, N. Wang, and S. Wen, "Elastoplastic fractal model for tangential contact damping energy dissipation of machine joint interfaces," *J. Mech. Eng.*, vol. 49, no. 12, pp. 43–49, 2013.
[13] X. Zhang, S. Wen, and G. Lan, "Fractal model for tangential contact damping of plane joint interfaces with simulation," *J. Xi'an Jiaotong Univ.*, vol. 45, no. 5, pp. 74–77, 2011.
[14] H. Li, H. Liu, and L. Yu, "Contact stiffness of rough mechanical joint surface," *J. Xi'an Jiaotong Univ.*, vol. 45, no. 6, pp. 69–74, 2011.
[15] X. Li, W. Wang, and M. Zhao, "Fractal prediction model for tangential contact damping of joint surface considering friction factors and its simulation," *J. Mech. Eng.*, vol. 48, no. 23, pp. 46–50, 2012.
[16] X. Zhang and S. Wen, "A fractal model of tangential contact stiffness of joint surfaces based on the contact fractal theory," *Trans. Chin. Soc. Agricult. Machinery*, vol. 33, no. 3, pp. 91–93, 2002.
[17] W. Wang, J. Wu, and Z. Gao, "A calculation model for tangential contact damping for mechine joint interfaces," *Acta Mechanica Sinica*, vol. 50, no. 3, pp. 633–642, 2018.
[18] H. Xiao, Y. Sun, J. Xu, and Y. Shao, "A calculation model for the normal contact stiffness of rough surface in mixed lubrication," *J. Vib. Shock*, vol. 37, no. 24, pp. 106–114, 2018.
[19] Y. Sun, H. Xiao, J. Xu, and W. Yu, "Study on the normal contact stiffness of the fractal rough surface in mixed lubrication," *Proc. Inst. Mech. Eng., J, J. Eng. Tribol.*, vol. 232, no. 12, pp. 1604–1617, Dec. 2018.
[20] L. Li, Q. Q. Yun, and Z. Q. Li, "Contact characteristics of joint surfaces considering bulk substrate deformation in mixed lubrication," *J. Vib., Meas. Diagnosis*, vol. 39, no. 5, pp. 953–959, 2019.
[21] L. Li, Y. X. Pei, and X. H. Shi, "Normal contact stiffness of machine joint surfaces under mixed lubrication state," *J. Vib. Shock*, vol. 39, no. 3, pp. 16–23, 2020.
[22] X. Y. Wen, X. Zhang, and W. B. Tan, "Study on the normal contact stiffness of the 3D fractal rough surface in mixed lubrication," *J. Mach. Tools Autom.*, vol. 2020, no. 11, pp. 49–53, 2020.
[23] G. Z. Gao, Z. X. Lu, and W. P. Fu, "Theoretical model and experimental analysis of normal dynamic contact stiffness and damping of solid-liquid mechanical joint," *Acta Mechanica Solida Sinica*, vol. 42, no. 6, pp. 682–696, 2021.
[24] C. Zhou, Z. Xiao, S. Chen, and X. Han, "Normal and tangential oil film stiffness of modified spur gear with non-Newtonian elastohydrodynamic lubrication," *Tribol. Int.*, vol. 109, pp. 319–327, May 2017.
[25] C. Zhou and Z. Xiao, "Stiffness and damping models for the oil film in line contact elastohydrodynamic lubrication and applications in the gear drive," *Appl. Math. Model.*, vol. 61, pp. 634–649, Sep. 2018.
[26] L. X. Peng, Z. Q. Gao, Z. Y. Ban, F. Gao, and W. P. Fu, "Dynamic tangential contact stiffness and damping model of the solid–liquid interface," *Machines*, vol. 10, pp. 1–26, Jan. 2022.
[27] R. S. Dwyer-Joyce, T. Reddyhoff, and J. Zhu, "Ultrasonic measurement for film thickness and solid contact in elastohydrodynamic lubrication," *J. Tribol.*, vol. 133, no. 3, pp. 407–411, Jul. 2011.
[28] P. Ren, L. H. Wang, and C. F. Wang, "Experimental study on normal dynamic contact stiffnesses of trail interfaces under lubrications," *China Mech. Eng.*, vol. 29, no. 7, pp. 811–816, 2018.
[29] C. N. Qu, L. S. Wu, Y. C. Xiao, and S. H. Zhang, "Summary of guideway technology research on machine tools," *Manuf. Technol. Mach. Tool*, vol. 2012, no. 1, pp. 30–36, 2012.
[30] R. L. Jackson, R. S. Duvvuru, H. Meghani, and M. Mahajan, "An analysis of elasto-plastic sliding spherical asperity interaction," *Wear*, vol. 262, nos. 1–2, pp. 210–219, Jan. 2007.
[31] M. H. Korayem and M. Zakeri, "Sensitivity analysis of nanoparticles pushing critical conditions in 2-D controlled nanomanipulation based on AFM," *Int. J. Adv. Manuf. Technol.*, vol. 41, nos. 7–8, pp. 714–726, Apr. 2009.
[32] K. Daeinabi and M. H. Korayem, "Indentation analysis of nano-particle using nano-contact mechanics models during nano-manipulation based on atomic force microscopy," *J. Nanopart. Res.*, vol. 13, no. 3, pp. 1075–1091, Mar. 2011.
[33] M. H. Korayem and M. Taheri, "Modeling of various contact theories for the manipulation of different biological micro/nanoparticles based on AFM," *J. Nanopart. Res.*, vol. 16, no. 1, pp. 1–13, Jan. 2014.
[34] M. Shisode, J. Hazrati, T. Mishra, M. de Rooij, and T. van den Boogaard, "Mixed lubrication friction model including surface texture effects for sheet metal forming," *J. Mater. Process. Technol.*, vol. 291, May 2021, Art. no. 117035.
[35] X. Shi, A. Wu, C. Jin, and S. Qu, "Thermomechanical modeling and transient analysis of sliding contacts between an elastic–plastic asperity and a rigid isothermal flat," *Tribol. Int.*, vol. 81, pp. 53–60, Jan. 2015.
[36] D. B. Patil and M. Eriten, "Effects of interfacial strength and roughness on the static friction coefficient," *Tribol. Lett.*, vol. 56, no. 2, pp. 355–374, Nov. 2014.
[37] L. Chang, "A deterministic model for line-contact partial elastohydrodynamic lubrication," *Tribol. Int.*, vol. 28, no. 2, pp. 75–84, Mar. 1995.
[38] Y.-Z. Hu and D. Zhu, "A full numerical solution to the mixed lubrication in point contacts," *J. Tribol.*, vol. 122, no. 1, pp. 1–9, Jan. 2000.
[39] A. R. Savkoor, "Mechanics of sliding friction of elastomers," *Wear*, vol. 113, no. 1, pp. 37–60, Dec. 1986.
[40] K. L. Johnson, *Contact Mechanics*. Cambridge, U.K.: Cambridge Univ. Press, 1985.
[41] J. M. Mattice, A. G. Lau, M. L. Oyen, and R. W. Kent, "Spherical indentation load-relaxation of soft biological tissues," *J. Mater. Res.*, vol. 21, no. 8, pp. 2005–2010, 2006.
[42] R. D. Mindlin and H. Deresiewicz, "Elastic spheres in contact under varying oblique forces," *J. Appl. Mech.*, vol. 20, no. 3, pp. 327–344, Sep. 1953.
[43] R. A. Schapery, "A theory of crack initiation and growth in viscoelastic media," *Int. J. Fract.*, vol. 11, no. 4, pp. 549–562, Aug. 1975.
[44] C. Wu and L. Zheng, "An average Reynolds equation for partial film lubrication with a contact factor," *J. Tribol.*, vol. 111, no. 1, pp. 188–191, Jan. 1989.
[45] S. Z. Wen and P. Huang, *Principles of Friction*, 2nd ed. Beijing, China: Tsinghua Univ. Press, 2002.
[46] L. Zheng, *Principles of Friction*. Beijing, China: Higher Educ. Press, 1994.
[47] X. Shi and A. A. Polycarpou, "Measurement and modeling of normal contact stiffness and contact damping at the Meso scale," *J. Vib. Acoust.*, vol. 127, no. 1, pp. 52–60, Feb. 2005.
[48] C. Ma, Y. Duan, B. Yu, J. Sun, and Q. Tu, "The comprehensive effect of surface texture and roughness under hydrodynamic and mixed lubrication conditions," *Proc. Inst. Mech. Eng., J, J. Eng. Tribol.*, vol. 231, no. 10, pp. 1307–1319, Oct. 2017.
[49] M. Gonzalez-Valadez, R. S. Dwyer-Joyce, and R. Lewis, "Ultrasonic reflection from mixed liquid-solid contacts and the determination of interface stiffness," *Tribol. Interface Eng. Ser.*, vol. 48, pp. 313–320, 2005.
[50] Z. W. Hu, K. Liu, and K. Liu, "Influence of surface topography deformation on friction at sliding contact interface in metal forming," *Tribology*, vol. 35, no. 4, pp. 368–377, 2015.
[51] M. Z. Shao, "Research on friction mechanism and testing device for plastic deformation of metal sheet," M.S. thesis, Shandong Univ., Jinan, China, 2021.
[52] B. Zhao, F. Wu, K. Sun, X. Mu, Y. Zhang, and Q. Sun, "Study on tangential stiffness nonlinear softening of bolted joint in friction-sliding process," *Tribol. Int.*, vol. 156, Apr. 2021, Art. no. 106856, doi: 10.1016/j.triboint.2021.106856.
[53] M. Rusli and M. Okuma, "Effect of surface topography on mode-coupling model of dry contact sliding systems," *J. Sound Vib.*, vol. 308, nos. 3–5, pp. 721–734, Dec. 2007.
[54] J. B. Luan, "Multi-scale simulation of high-speed dry sliding friction process on double rough surfaces," Ph.D. dissertation, Yanshan Univ., Qinhuangdao, China, 2021.
[55] F. Van De Velde and P. De Baets, "The relation between friction force and relative speed during the slip-phase of a stick-slip cycle," *Wear*, vol. 219, no. 2, pp. 220–226, Sep. 1998.

LIXIA PENG received the M.S. degree from the Lanzhou University of Technology, Lanzhou, China, in 2009. She is currently pursuing the Ph.D. degree majoring in mechanical engineering with the Xi'an University of Technology. She is also a Professor with Xi'an International University. Her primary research interests include intelligent robotics and mechanical system dynamics.

ZHAOYANG BAN received the bachelor's degree in mechanical design, manufacturing and automation from the Xi'an University of Technology, Shaanxi, China, in 2018, where he is currently pursuing the master's degree majoring in mechanical engineering. His research interest includes mechanical system dynamics.

ZHIQIANG GAO received the Ph.D. degree from the Xi'an University of Technology, Xi'an, China, in 2018. His research interests include mechanical optimization and dynamics analysis, and the intelligent loading and unloading system of robot.

WEIPING FU received the Ph.D. degree from Xi'an Jiaotong University, Xi'an, China, in 1996. He is currently a Professor with the Xi'an University of Technology, Xi'an. He was the Standing Director of Shaanxi Vibration Engineering Society and Xi'an Vibration and Noise Society. He is a member of China Computer Society. His research interests include intelligent robot, logistics automation, and intelligent manufacturing.

FENG GAO received the Ph.D. degree from the Xi'an University of Technology, Xi'an, China, in 2001. He is currently a Professor with the Xi'an University of Technology. His research interests include CNC equipment design and control technology, the virtual prototype simulation technology of CNC machine tools, the on-machine testing technology of CNC machine tools, and error compensation theory.

WEN WANG received the B.S. degree from Nanchang Hangkong University, Nanchang, China, in 1987, and the M.S. and Ph.D. degrees from the Xi'an University of Technology, Xi'an, China, in 2004 and 2010, respectively. She is currently a Professor with the Xi'an University of Technology. Her current research interests include intelligent robotics and modern logistics system engineering.